

# Dynamic imaging and quantitative analysis of cranial neural tube closure in the mouse embryo using optical coherence tomography

SHANG WANG,<sup>1,5</sup> MONICA D. GARCIA,<sup>1,5</sup> ANDREW L. LOPEZ III,<sup>1</sup> PAUL A. OVERBEEK,<sup>2</sup> KIRILL V. LARIN,<sup>1,3,4</sup> AND IRINA V. LARINA<sup>1,\*</sup>

<sup>1</sup>Department of Molecular Physiology and Biophysics, Baylor College of Medicine, One Baylor Plaza, Houston, TX 77030, USA

<sup>2</sup>Department of Molecular & Cellular Biology, Baylor College of Medicine, One Baylor Plaza, Houston, TX 77030, USA

<sup>3</sup>Interdisciplinary Laboratory of Biophotonics, Tomsk State University, Tomsk, Russia

<sup>4</sup>Department of Biomedical Engineering, University of Houston, 3605 Cullen Blvd., Houston, TX 77204, USA

<sup>5</sup>Equal Contribution

\*[larina@bcm.edu](mailto:larina@bcm.edu)

**Abstract:** Neural tube closure is a critical feature of central nervous system morphogenesis during embryonic development. Failure of this process leads to neural tube defects, one of the most common forms of human congenital defects. Although molecular and genetic studies in model organisms have provided insights into the genes and proteins that are required for normal neural tube development, complications associated with live imaging of neural tube closure in mammals limit efficient morphological analyses. Here, we report the use of optical coherence tomography (OCT) for dynamic imaging and quantitative assessment of cranial neural tube closure in live mouse embryos in culture. Through time-lapse imaging, we captured two neural tube closure mechanisms in different cranial regions, zipper-like closure of the hindbrain region and button-like closure of the midbrain region. We also used OCT imaging for phenotypic characterization of a neural tube defect in a mouse mutant. These results suggest that the described approach is a useful tool for live dynamic analysis of normal neural tube closure and neural tube defects in the mouse model.

© 2016 Optical Society of America

**OCIS codes:** (170.3880) Medical and biological imaging; (170.4500) Optical coherence tomography; (170.6920) Time-resolved imaging.

## References and links

1. R. J. Lemire, "Neural tube defects," *JAMA* **259**(4), 558–562 (1988).
2. L. D. Botto, C. A. Moore, M. J. Khoury, and J. D. Erickson, "Neural-Tube Defects," *N. Engl. J. Med.* **341**(20), 1509–1519 (1999).
3. A. Osterhues, N. S. Ali, and K. B. Michels, "The Role of Folic Acid Fortification in Neural Tube Defects: A Review," *Crit. Rev. Food Sci. Nutr.* **53**(11), 1180–1190 (2013).
4. G. C. Schoenwolf and J. L. Smith, "Mechanisms of neurulation: traditional viewpoint and recent advances," *Development* **109**(2), 243–270 (1990).
5. J.-F. Colas and G. C. Schoenwolf, "Towards a cellular and molecular understanding of neurulation," *Dev. Dyn.* **221**(2), 117–145 (2001).
6. M. V. S. R. Group; MRC Vitamin Study Research Group, "Prevention of neural tube defects: Results of the Medical Research Council Vitamin Study," *Lancet* **338**(8760), 131–137 (1991).
7. G. Morriss-Kay, H. Wood, and W. H. Chen, "Normal neurulation in mammals," *Ciba Foundation symposium* **181**, 51–63 (1994).
8. L. R. Campbell, D. H. Dayton, and G. S. Sohal, "Neural tube defects: A review of human and animal studies on the etiology of neural tube defects," *Teratology* **34**(2), 171–187 (1986).
9. Y. Yamaguchi and M. Miura, "How to form and close the brain: insight into the mechanism of cranial neural tube closure in mammals," *Cell. Mol. Life Sci.* **70**(17), 3171–3186 (2013).
10. D. M. Juriloff and M. J. Harris, "Mouse models for neural tube closure defects," *Hum. Mol. Genet.* **9**(6), 993–1000 (2000).

11. M. J. Harris and D. M. Juriloff, "Mouse mutants with neural tube closure defects and their role in understanding human neural tube defects," *Birth Defects Res. A Clin. Mol. Teratol.* **79**(3), 187–210 (2007).
12. A. J. Copp and N. D. E. Greene, "Genetics and development of neural tube defects," *J. Pathol.* **220**(2), 217–230 (2010).
13. V. Massa, D. Savery, P. Ybot-Gonzalez, E. Ferraro, A. Rongvaux, F. Cecconi, R. Flavell, N. D. E. Greene, and A. J. Copp, "Apoptosis is not required for mammalian neural tube closure," *Proc. Natl. Acad. Sci. U.S.A.* **106**(20), 8233–8238 (2009).
14. S. G. McShane, M. A. Molè, D. Savery, N. D. E. Greene, P. P. L. Tam, and A. J. Copp, "Cellular basis of neuroepithelial bending during mouse spinal neural tube closure," *Dev. Biol.* **404**(2), 113–124 (2015).
15. R. Massarwa and L. Niswander, "In toto live imaging of mouse morphogenesis and new insights into neural tube closure," *Development* **140**(1), 226–236 (2013).
16. M. Rădulescu, E. C. Ulmeanu, M. Nedelea, and A. Oncescu, "Prenatal ultrasound diagnosis of neural tube defects. Pictorial essay," *Med. Ultrason.* **14**(2), 147–153 (2012).
17. D. H. Turnbull, T. S. Bloomfield, H. S. Baldwin, F. S. Foster, and A. L. Joyner, "Ultrasound backscatter microscope analysis of early mouse embryonic brain development," *Proc. Natl. Acad. Sci. U.S.A.* **92**(6), 2239–2243 (1995).
18. D. H. Turnbull, "In utero ultrasound backscatter microscopy of early stage mouse embryos," *Comput. Med. Imaging Graph.* **23**(1), 25–31 (1999).
19. E. A. V. Jones, D. Crotty, P. M. Kulesa, C. W. Waters, M. H. Baron, S. E. Fraser, and M. E. Dickinson, "Dynamic in vivo imaging of postimplantation mammalian embryos using whole embryo culture," *Genesis* **34**(4), 228–235 (2002).
20. J. M. Rhee, M. K. Pirity, C. S. Lackan, J. Z. Long, G. Kondoh, J. Takeda, and A. K. Hadjantonakis, "In vivo imaging and differential localization of lipid-modified GFP-variant fusions in embryonic stem cells and mice," *Genesis* **44**(4), 202–218 (2006).
21. C. Pyrgaki, P. Trainor, A. K. Hadjantonakis, and L. Niswander, "Dynamic imaging of mammalian neural tube closure," *Dev. Biol.* **344**(2), 941–947 (2010).
22. Y. Yamaguchi, N. Shinotsuka, K. Nonomura, K. Takemoto, K. Kuida, H. Yosida, and M. Miura, "Live imaging of apoptosis in a novel transgenic mouse highlights its role in neural tube closure," *J. Cell Biol.* **195**(6), 1047–1060 (2011).
23. D. Huang, E. A. Swanson, C. P. Lin, J. S. Schuman, W. G. Stinson, W. Chang, M. R. Hee, T. Flotte, K. Gregory, C. A. Puliafito, and et, "Optical coherence tomography," *Science* **254**(5035), 1178–1181 (1991).
24. S. A. Boppart, "Optical coherence tomography: technology and applications for neuroimaging," *Psychophysiology* **40**(4), 529–541 (2003).
25. U. Baran and R. K. Wang, "Review of optical coherence tomography based angiography in neuroscience," *Neurophotonics* **3**(1), 010902 (2016).
26. J. Men, Y. Huang, J. Solanki, X. Zeng, A. Alex, J. Jerwick, Z. Zhang, R. E. Tanzi, A. Li, and C. Zhou, "Optical Coherence Tomography for Brain Imaging and Developmental Biology," *IEEE J. Sel. Top. Quantum Electron.* **22**(4), 120–132 (2016).
27. G. H. Karunamuni, S. Gu, M. R. Ford, L. M. Peterson, P. Ma, Y. T. Wang, A. M. Rollins, M. W. Jenkins, and M. Watanabe, "Capturing structure and function in an embryonic heart with biophotonic tools," *Front. Physiol.* **5**, 351 (2014).
28. P. Hahn, J. Migacz, R. O'Connell, R. S. Maldonado, J. A. Izatt, and C. A. Toth, "The Use of Optical Coherence Tomography in Intraoperative Ophthalmic Imaging," *Ophthalmic Surg. Lasers Imaging* **42**(4 Suppl), S85–S94 (2011).
29. H. G. Bezerra, M. A. Costa, G. Guagliumi, A. M. Rollins, and D. I. Simon, "Intracoronary Optical Coherence Tomography: A Comprehensive Review Clinical and Research Applications," *JACC Cardiovasc. Interv.* **2**(11), 1035–1046 (2009).
30. F. T. Nguyen, A. M. Zysk, E. J. Chaney, J. G. Kotynek, U. J. Oliphant, F. J. Bellafiore, K. M. Rowland, P. A. Johnson, and S. A. Boppart, "Intraoperative Evaluation of Breast Tumor Margins with Optical Coherence Tomography," *Cancer Res.* **69**(22), 8790–8796 (2009).
31. A. M. Davis, S. A. Boppart, F. Rothenberg, and J. A. Izatt, "OCT Applications in Developmental Biology," in *Optical Coherence Tomography: Technology and Applications*, W. Drexler, and J. G. Fujimoto, eds. (Springer Berlin Heidelberg, Berlin, Heidelberg, 2008), pp. 919–959.
32. R. Raghunathan, M. Singh, M. E. Dickinson, and K. V. Larin, "Optical coherence tomography for embryonic imaging: a review," *J. Biomed. Opt.* **21**(5), 050902 (2016).
33. J. C. Burton, S. Wang, C. A. Stewart, R. R. Behringer, and I. V. Larina, "High-resolution three-dimensional in vivo imaging of mouse oviduct using optical coherence tomography," *Biomed. Opt. Express* **6**(7), 2713–2723 (2015).
34. S. A. Boppart, G. J. Tearney, B. E. Bouma, J. F. Southern, M. E. Brezinski, and J. G. Fujimoto, "Noninvasive assessment of the developing *Xenopus* cardiovascular system using optical coherence tomography," *Proc. Natl. Acad. Sci. U.S.A.* **94**(9), 4256–4261 (1997).
35. T. M. Yelbuz, M. A. Choma, L. Thrane, M. L. Kirby, and J. A. Izatt, "Optical coherence tomography: a new high-resolution imaging technology to study cardiac development in chick embryos," *Circulation* **106**(22), 2771–2774 (2002).

36. W. Luo, D. L. Marks, T. S. Ralston, and S. A. Boppart, "Three-dimensional optical coherence tomography of the embryonic murine cardiovascular system," *J. Biomed. Opt.* **11**(2), 021014 (2006).
37. M. W. Jenkins, O. Q. Chughtai, A. N. Basavanahally, M. Watanabe, and A. M. Rollins, "In vivo gated 4D imaging of the embryonic heart using optical coherence tomography," *J. Biomed. Opt.* **12**(3), 030505 (2007).
38. A. Liu, R. Wang, K. L. Thornburg, and S. Rugonyi, "Efficient postacquisition synchronization of 4-D nongated cardiac images obtained from optical coherence tomography: application to 4-D reconstruction of the chick embryonic heart," *J. Biomed. Opt.* **14**, 044020 (2009).
39. S. Wang, M. Singh, A. L. Lopez 3rd, C. Wu, R. Raghunathan, A. Schill, J. Li, K. V. Larin, and I. V. Larina, "Direct four-dimensional structural and functional imaging of cardiovascular dynamics in mouse embryos with 1.5 MHz optical coherence tomography," *Opt. Lett.* **40**(20), 4791–4794 (2015).
40. P. Li, X. Yin, L. Shi, A. Liu, S. Rugonyi, and R. Wang, "Measurement of strain and strain rate in embryonic chick heart in vivo using spectral domain optical coherence tomography," *IEEE Trans. Biomed. Eng.* **58**(8), 2333–2338 (2011).
41. A. Liu, X. Yin, L. Shi, P. Li, K. L. Thornburg, R. Wang, and S. Rugonyi, "Biomechanics of the Chick Embryonic Heart Outflow Tract at HH18 Using 4D Optical Coherence Tomography Imaging and Computational Modeling," *PLoS One* **7**(7), e40869 (2012).
42. L. M. Peterson, M. W. Jenkins, S. Gu, L. Barwick, M. Watanabe, and A. M. Rollins, "4D shear stress maps of the developing heart using Doppler optical coherence tomography," *Biomed. Opt. Express* **3**(11), 3022–3032 (2012).
43. M. W. Jenkins, L. Peterson, S. Gu, M. Garghesha, D. L. Wilson, M. Watanabe, and A. M. Rollins, "Measuring hemodynamics in the developing heart tube with four-dimensional gated Doppler optical coherence tomography," *J. Biomed. Opt.* **15**, 066022 (2010).
44. M. Midgett, V. K. Chivukula, C. Dorn, S. Wallace, and S. Rugonyi, "Blood flow through the embryonic heart outflow tract during cardiac looping in HH13–HH18 chicken embryos," *J. R. Soc. Interface* **12**(111), 20150652 (2015).
45. S. Wang, D. S. Lakomy, M. D. Garcia, A. L. Lopez 3rd, K. V. Larin, and I. V. Larina, "Four-dimensional live imaging of hemodynamics in mammalian embryonic heart with Doppler optical coherence tomography," *J. Biophotonics* **9**(8), 837–847 (2016).
46. A. Alex, A. Li, X. Zeng, R. E. Tate, M. L. McKee, D. E. Capen, Z. Zhang, R. E. Tanzi, and C. Zhou, "A Circadian Clock Gene, *Cry*, Affects Heart Morphogenesis and Function in *Drosophila* as Revealed by Optical Coherence Microscopy," *PLoS One* **10**(9), e0137236 (2015).
47. A. Li, O. O. Ahsen, J. J. Liu, C. Du, M. L. McKee, Y. Yang, W. Wasco, C. H. Newton-Cheh, C. J. O'Donnell, J. G. Fujimoto, C. Zhou, and R. E. Tanzi, "Silencing of the *Drosophila* ortholog of *SOX5* in heart leads to cardiac dysfunction as detected by optical coherence tomography," *Hum. Mol. Genet.* **22**(18), 3798–3806 (2013).
48. A. L. Lopez 3rd, S. Wang, K. V. Larin, P. A. Overbeek, and I. V. Larina, "Live four-dimensional optical coherence tomography reveals embryonic cardiac phenotype in mouse mutant," *J. Biomed. Opt.* **20**(9), 090501 (2015).
49. G. Karunamuni, S. Gu, Y. Q. Doughman, A. I. Noonan, A. M. Rollins, M. W. Jenkins, and M. Watanabe, "Using optical coherence tomography to rapidly phenotype and quantify congenital heart defects associated with prenatal alcohol exposure," *Dev. Dyn.* **244**(4), 607–618 (2015).
50. P. Ma, S. Gu, G. H. Karunamuni, M. W. Jenkins, M. Watanabe, and A. M. Rollins, "Cardiac neural crest ablation results in early endocardial cushion and hemodynamic flow abnormalities," *Am. J. Physiol. Heart Circ. Physiol.* **311**(5), H1150–H1159 (2016).
51. M. Midgett, S. Goenezen, and S. Rugonyi, "Blood flow dynamics reflect degree of outflow tract banding in Hamburger-Hamilton stage 18 chicken embryos," *J. R. Soc. Interface* **11**(100), 20140643 (2014).
52. A. Alex, A. Li, R. E. Tanzi, and C. Zhou, "Optogenetic pacing in *Drosophila melanogaster*," *Sci. Adv.* **1**(9), e1500639 (2015).
53. I. V. Larina, K. V. Larin, M. E. Dickinson, and M. Liebling, "Sequential Turning Acquisition and Reconstruction (STAR) method for four-dimensional imaging of cyclically moving structures," *Biomed. Opt. Express* **3**(3), 650–660 (2012).
54. P. M. Kulkarni, N. Rey-Villamizar, A. Merouane, N. Sudheendran, S. Wang, M. Garcia, I. V. Larina, B. Roysam, and K. V. Larin, "Algorithms for improved 3-D reconstruction of live mammalian embryo vasculature from optical coherence tomography data," *Quant. Imaging Med. Surg.* **5**(1), 125–135 (2015).
55. S. H. Syed, A. J. Coughlin, M. D. Garcia, S. Wang, J. L. West, K. V. Larin, and I. V. Larina, "Optical coherence tomography guided microinjections in live mouse embryos: high-resolution targeted manipulation for mouse embryonic research," *J. Biomed. Opt.* **20**(5), 051020 (2015).
56. S. Wang, J. C. Burton, R. R. Behringer, and I. V. Larina, "In vivo micro-scale tomography of ciliary behavior in the mammalian oviduct," *Sci. Rep.* **5**, 13216 (2015).
57. M. Garcia, A. Lopez III, K. Larin, and I. Larina, "Imaging of Cardiovascular Development in Mammalian Embryos Using Optical Coherence Tomography," in *Vascular Morphogenesis*, D. Ribatti, ed. (Springer New York, 2015), pp. 151–161.
58. A. Lopez III, M. Garcia, M. Dickinson, and I. Larina, "Live Confocal Microscopy of the Developing Mouse Embryonic Yolk Sac Vasculature," in *Vascular Morphogenesis*, D. Ribatti, ed. (Springer New York, 2015), pp. 163–172.

59. M. D. Garcia, R. S. Udan, A.-K. Hadjantonakis, and M. E. Dickinson, "Preparation of Rat Serum for Culturing Mouse Embryos," *Cold Spring Harbor Protocols* **2011**, pdb.prot5593 (2011).
60. T. Gridley, P. Soriano, and R. Jaenisch, "Insertional versus targeted mutagenesis in mice," *New Biol.* **3**(11), 1025–1034 (1991).
61. A. Ashe, N. C. Butterfield, L. Town, A. D. Courtney, A. N. Cooper, C. Ferguson, R. Barry, F. Olsson, K. F. Liem, Jr., R. G. Parton, B. J. Wainwright, K. V. Anderson, E. Whitelaw, and C. Wicking, "Mutations in mouse *lft144* model the craniofacial, limb and rib defects in skeletal ciliopathies," *Hum. Mol. Genet.* **21**(8), 1808–1823 (2012).
62. A. F. Fercher, W. Drexler, C. K. Hitzenberger, and T. Lasser, "Optical coherence tomography - principles and applications," *Rep. Prog. Phys.* **66**(2), 239–303 (2003).
63. L. Liu, J. A. Gardecki, S. K. Nadkarni, J. D. Toussaint, Y. Yagi, B. E. Bouma, and G. J. Tearney, "Imaging the subcellular structure of human coronary atherosclerosis using micro-optical coherence tomography," *Nat. Med.* **17**(8), 1010–1014 (2011).
64. C. Zhou, Y. Wang, A. D. Aguirre, T.-H. Tsai, D. W. Cohen, J. L. Connolly, and J. G. Fujimoto, "Ex vivo imaging of human thyroid pathology using integrated optical coherence tomography and optical coherence microscopy," *J. Biomed. Opt.* **15**(1), 016001 (2010).
65. C. Zhou, D. W. Cohen, Y. Wang, H.-C. Lee, A. E. Mondelblatt, T.-H. Tsai, A. D. Aguirre, J. G. Fujimoto, and J. L. Connolly, "Integrated Optical Coherence Tomography and Microscopy for Ex Vivo Multiscale Evaluation of Human Breast Tissues," *Cancer Res.* **70**(24), 10071–10079 (2010).
66. W. Wieser, W. Draxinger, T. Klein, S. Karpf, T. Pfeiffer, and R. Huber, "High definition live 3D-OCT in vivo: design and evaluation of a 4D OCT engine with 1 GVoxel/s," *Biomed. Opt. Express* **5**(9), 2963–2977 (2014).

## 1. Introduction

Neural tube defects (NTDs) are common congenital defects, with an occurrence rate of 1 in 1000 pregnancies in the United States [1, 2]. Although introduction of folic acid fortification has led to a significant reduction of NTDs, this inborn disease still persists and the etiology is largely unknown [3]. Despite numerous studies on neurulation in various animal models, the developmental perturbations that induce mammalian NTDs remain poorly defined [4, 5], limiting progress in formulating strategies to prevent human NTDs [6]. Neurulation in mammals involves the formation, shaping, and bending of the neural plate and the closure of the neural folds [7]. Defects in cranial neural tube closure can result in exencephaly in rodents and possibly anencephaly in human [8, 9].

The mouse is a superior model for investigations of central nervous system development due to the widely available genetic tools and NTD models [10]. Advances in the molecular biology have led to the identification of genes and molecular pathways relevant to cranial neural tube closure and NTDs [11, 12]. However, most studies rely on histology for morphologic analysis. Histology provides only static images, and therefore has intrinsic limitations in regards to capturing the dynamic aspects of neural tube morphogenesis. In addition to the investigations at the molecular level, studies of this morphogenetic event at the tissue and cellular levels are also highly critical for reaching an improved understanding of neurulation and NTDs [13–15]. Nevertheless, available imaging tools allowing for live time-resolved assessment of the cranial neural tube closure in the mouse embryo are limited, preventing the analysis of mammalian neurulation from a dynamic point of view.

While ultrasonic imaging is currently the most used approach for clinical fetal neural tube examination [16], its application for approaching neurulation in the mouse model has gained limited success, due to the relatively low spatial resolution (down to tens of microns) that is difficult to resolve detailed structure of the neural tube at early developmental stages [17, 18]. Optical imaging techniques with improved spatial resolution have been employed to visualize and study cranial neural tube closure in live mouse embryos. With static culturing of the early-stage mouse embryo, confocal microscopy was utilized to acquire time-lapse videos of neural tube closure in the hindbrain region [19]. Also, with a transgenic mouse line where the cell membrane is fluorescently labeled [20], confocal imaging was employed in live mouse embryo culture to assess cell-cell interactions during closure of the cranial neural tube [21] and to assess the disrupted closure in a NTD model [15]. Using fast-scanning confocal microscope, functional imaging of apoptosis during cranial neural tube closure of live cultured mouse embryos was achieved based on a genetically encoded fluorescence resonance

energy transfer reporter [22]. Although the micron and sub-micron spatial resolution of confocal microscopy is advantageous for observing cellular details during mouse neurulation, the limited imaging depth requires the embryo to be dissected out from the yolk sac with the head folds directly exposed and also makes it difficult to keep the target region within the field of view during the turning of the embryo. In addition, transgenic reporters are necessary due to the poor endogenous imaging contrast.

Optical coherence tomography (OCT) employs backscattered light from tissue samples to form three-dimensional (3D) structural images where no exogenous contrast agent is needed [23]. Utilizing low-coherence light in the near-infrared region, OCT features a microscale spatial resolution with an imaging depth at millimeter level in scattering tissues [24], bridging the gap of imaging scales between the confocal and acoustic imaging techniques. This unique spatial imaging scale of OCT has enabled applications ranging from biomedical research [25–27] to clinical diagnosis and monitoring [28–30]. Embryology is a major research area where OCT shows great promise as a high-resolution unlabeled imaging tool [31–33]. With the primary focus on the cardiovascular development and abnormalities, OCT has been reported able to reveal detailed structures of the embryonic heart comparable to histology [34–36], to capture four-dimensional dynamic cardiac activities [37–39], to quantify biomechanics of the heart tube [40–42], to assess cardiac hemodynamics [43–45], to characterize novel mutant heart phenotypes [46–48], and to investigate cardiac responses to physical and chemical manipulations [49–52]. Focusing on the mouse model, our group has combined OCT with live embryo culture to establish a number of structural and functional imaging methods [39, 45, 48, 53–55], suggesting an important role of OCT for *in vivo* analysis of the mammalian embryo. However, the feasibility of using OCT for live imaging of neurulation in the mouse embryo remains unexplored.

In this paper, we report the first application of OCT for live dynamic assessment of neural tube development. Specifically, we present time-lapse 3D OCT imaging of cranial neural tube closure in the live mouse embryo within the intact yolk sac. Our dynamic visualizations and quantitative analyses revealed distinct mechanisms of the neural tube closure in the hindbrain and midbrain regions. Also, we show that 3D OCT imaging provides a quantitative measure of an NTD in the *Wdr19* mutant model. Our results demonstrate that OCT can be used as an efficient imaging and characterization tool for live investigations of cranial neural tube closure in mouse models, which can open new opportunities for studying normal neurulation and NTDs.

## 2. Materials and methods

### 2.1 OCT system

A home-built spectral-domain OCT system was utilized in this study. Details of the OCT system were described in our previous work [56]. Briefly, the system employs a near-infrared laser with ~808 nm central wavelength and ~110 nm bandwidth. Relying on a fiber-based Michelson interferometer, the interference of light from the reference and sample arm is directed to a spectrometer with a high-speed line-field CMOS camera. Fast-Fourier transform is used to obtain the OCT intensity A-line from equally *k*-spaced interference fringes. The system has an axial resolution of ~5  $\mu\text{m}$  in tissue (refractive index of 1.4 assumed). The transverse resolution is measured to be ~4  $\mu\text{m}$ . A sensitivity of ~97 dB is achieved with a ~50  $\mu\text{m}$  optical path-length difference and an 18  $\mu\text{s}$  exposure time. Due to finite spatial sampling rate of the spectrometer, a sensitivity drop of ~4 dB is observed over ~1 mm in depth. A set of galvanometer mirrors is utilized for transverse scanning to acquire 3D data. With all 4096 pixels used from the camera, an A-line rate up to ~68 kHz can be reached, providing the flexibility for adjusting the volume size and the required time for acquiring one 3D data set. The sample arm of the OCT system was placed in an incubator (37 °C and 5% CO<sub>2</sub>), as shown in Fig. 1(A), for live embryonic imaging experiments.



## 2.2 Mouse embryo manipulations

All animal manipulation procedures involved in this work were approved by the Animal Care and Use Committee of the Baylor College of Medicine. All the experiments were carried out according to the approved protocols.

Timed matings were used to initiate pregnancies. Vaginal plugs were monitored, and the day a plug was found was counted as embryonic day 0.5 (E0.5). For live time-lapse imaging experiments of cranial neural tube closure, wild-type CD-1 mice were used. The embryos were dissected out from the uterus at early E8.5 (~6-8 somites) when the closure initiation sites were still open [12]. Live embryo culture on a stage was employed to maintain the development of the mouse embryo for OCT imaging [19, 57]. Embryos were dissected at 37 °C with the yolk sac intact in the dissection medium containing 89% DMEM/F12, 1% penicillin-streptomycin and 10% fetal bovine serum [58]. After dissection, the embryos were allowed to recover in a 37 °C incubator maintained at 5% CO<sub>2</sub> prior to imaging. For the prolonged time-lapse OCT imaging, home-made rat serum [59] was added to the dissection medium (1:4) to support embryo growth. To prevent any evaporation of the culture medium during the course of the experiment, a piece of thin Teflon film was placed on top of the medium, as shown in Fig. 1(A). The edge of the film was sealed by addition of mineral oil.

For phenotypic characterization experiments, the *Wdr19* mutant mouse line generated through insertional mutagenesis [48, 60] was used. Heterozygous mice that are viable and do not exhibit obvious defects were set up for mating. Embryos were dissected live at the stage of E8.5 (8-12 somites) when the closure of the head folds has already initiated. After imaging, the embryos were collected and genotyped with polymerase chain reaction [48].

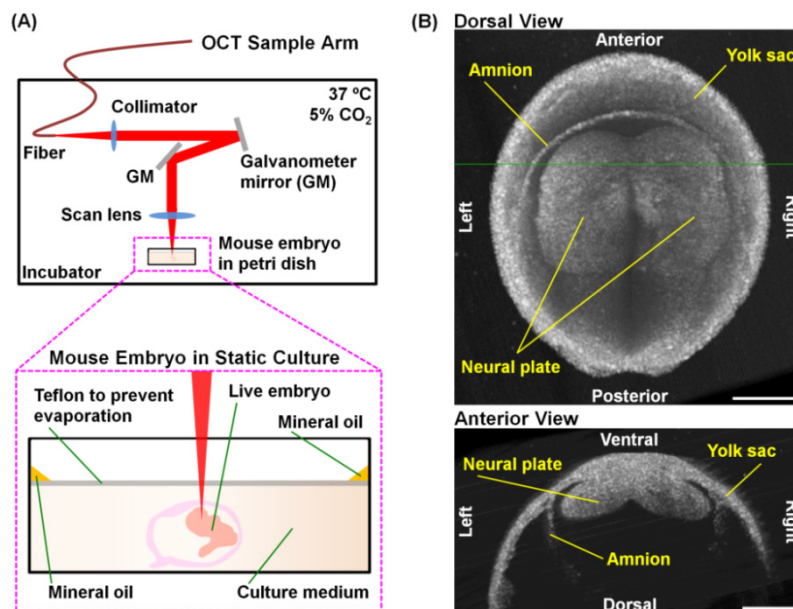


Fig. 1. Live mouse embryo culture combined with OCT imaging for analysis of cranial neural tube closure. (A) Setup of the OCT sample arm inside a humidified incubator for static mouse embryo culture (Top); An enlarged side view of the culturing setup for the mouse embryo where a transparent Teflon film is placed on top of the medium to avoid evaporation (Bottom). (B) An example of 3D OCT embryonic imaging with a live mouse embryo at the stage of early E8.0 when the neural plates are formed yet not bent. The green line in the dorsal view indicates the position where the anterior view is taken. Scale bars correspond to 200  $\mu$ m.

### 2.3 Imaging and quantitative assessment

For time-lapse imaging, continuous OCT 3D imaging was performed with the time scale set at 550 seconds temporal resolution for the four-dimensional data. The duration of the live imaging experiments was set for over 16 hours which covers the full events of cranial neural tube closure. Our imaging field of view of  $\sim 3$  mm in 3D ensured the head region of the mouse embryo within the intact yolk sac could always be visualized and no adjustment of imaging parameters was required throughout the experiments. An example for OCT structural imaging of the cranial region is shown in Fig. 1(B) with a live mouse embryo at the pre-somite stage (early E8.0). It can be seen that at this stage the neural plates have formed but bending is yet to occur. With the 3D OCT data, the cranial morphology can be well resolved.

For the characterization of the NTD in *Wdr19* mutants, live embryos within the intact yolk sac were placed in a cold  $1 \times$  PBS solution right before imaging. This temperature change inhibited heart contraction and significantly reduced the motion effect from the beating heart while preserving the structure of the whole embryo for imaging. Single 3D OCT imaging was performed on all embryos focusing on the forebrain region of the neural tube. For data analysis, the homozygous embryos were compared with the control where the wild-type and heterozygous littermates were grouped together. During our post processing with 3D OCT data, embryos showing a visually apparent turning were excluded from analysis to ensure the embryos from the control and the mutant groups were very close with respect to their developmental stages. A total of 20 embryos (10 for each group) were utilized for the analysis. For comparison, the effect size was calculated and a two-sample *t* test was used to determine the statistical significance.

The 3D visualization and the quantification of the distances between neural folds were conducted using Imaris software (Bitplane). All measurements were made in 3D, which were utilized for the time-resolved analysis of cranial neural tube closure and the comparative analysis of mutant brain phenotypes.

## 3. Results

The process of cranial neural tube closure in the live mouse embryo can be clearly visualized using time-lapse 3D OCT imaging, as shown in Fig. 2 and [Visualization 1](#). As annotated in Fig. 2(A), the forebrain, the midbrain and the hindbrain, as well as the pharyngeal arch can be easily located and well distinguished through the yolk sac. Over the  $\sim 16.8$  hours' duration of OCT imaging, the increase of the size of embryo and the remodeling of the yolk sac vasculature can be directly seen, as shown in Fig. 2(B), which indicates the growth and the development of the cultured embryo during the imaging. From Fig. 2(C), it can be seen that the head folds of the embryo are open when the imaging starts (0 hour) and the cranial neural tube is fully closed by the time of 13.75 hours. The closure of the head initiates at the junction of the forebrain and the midbrain (triangle, 2.75 hour) and, as the embryo is turning, neural tube closure gradually completes (5.5, 8.25 and 11 hour). The observed duration of the cranial closure agrees with the literature [15, 19], suggesting the feasibility of using OCT imaging and live embryo culture to study this important process of neurulation in the mouse model.

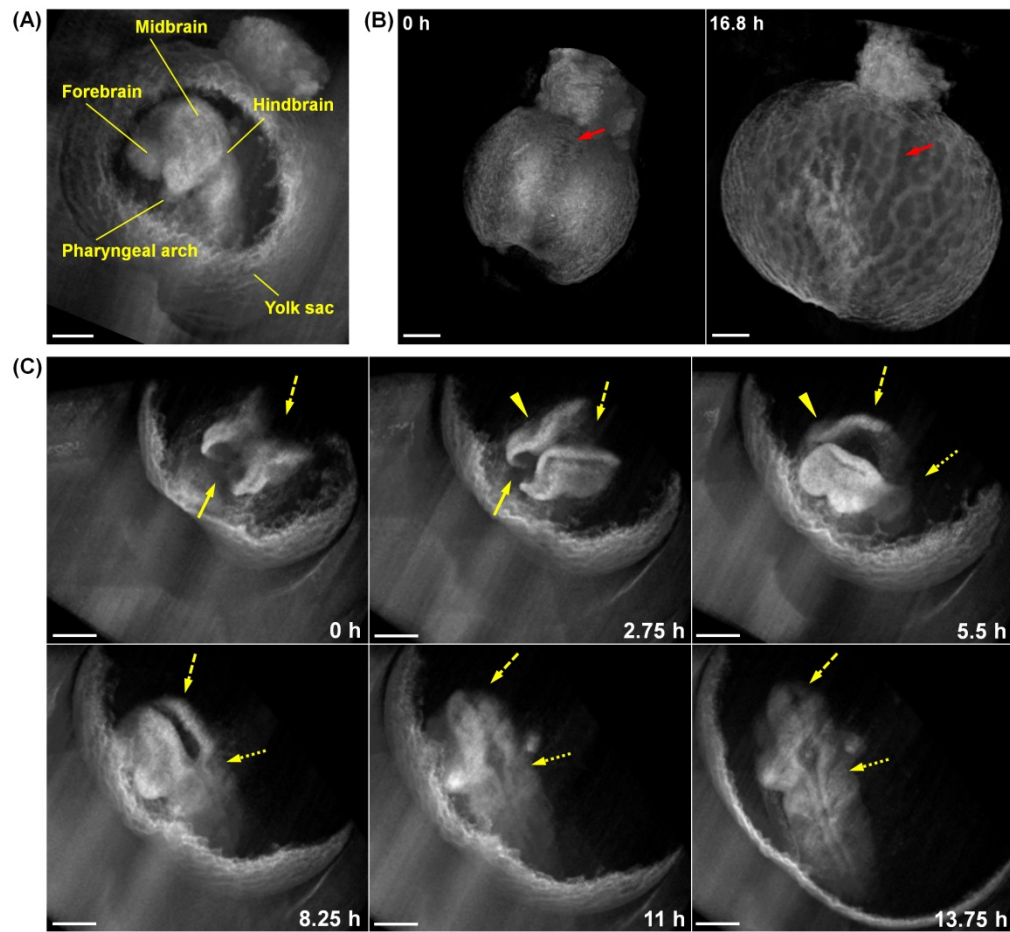


Fig. 2. Time-lapse 3D OCT imaging of the cranial neural tube closure in the mouse embryo for over 16 hours. (A) A 3D image of the mouse embryo shows the three major parts of the cranial region, the forebrain, the midbrain and the hindbrain. (B) 3D images of the mouse embryo at the beginning and ending time points of the imaging session show the size increase and the yolk sac vascular remodeling through development. The red arrows indicate the capillary plexus (left) and the remodeled blood vessels (right). (C) Representative frames from 3D OCT time-lapse demonstrate cranial neural tube closure while the embryo is turning (see [Visualization 1](#)). In the images of selected time points, the solid, dashed and dotted arrows point at forebrain, midbrain and hindbrain of the embryo, respectively, and the triangle points at a closure initiation site between the forebrain and midbrain. All scale bars correspond to 300  $\mu\text{m}$ . The time stamps of images correspond to [Visualization 1](#). The playback is 5000 times faster.

The embryonic hindbrain region was imaged during neural tube closure and this process was quantitatively assessed. As shown in Fig. 3(A) and [Visualization 2](#), the closure of the hindbrain region is driven by a continuous sequential fusion of the neural folds from the posterior side to the anterior side, as indicated by the red arrows. This progression of fusion is generally described as zipper-like closure of the neural tube. Measurements of the distance between neural folds at five selected line positions from the hindbrain region are plotted with respect to time in Fig. 3(B). The locations of the lines L1-L5 are shown in the first image (0 minute) of Fig. 3(A). It is obvious that the closure occurs in a sequential order from line L1 to line L5 with time delays of  $\sim 18$ -28 minutes between each position, following the zipper-like mechanism of closure.



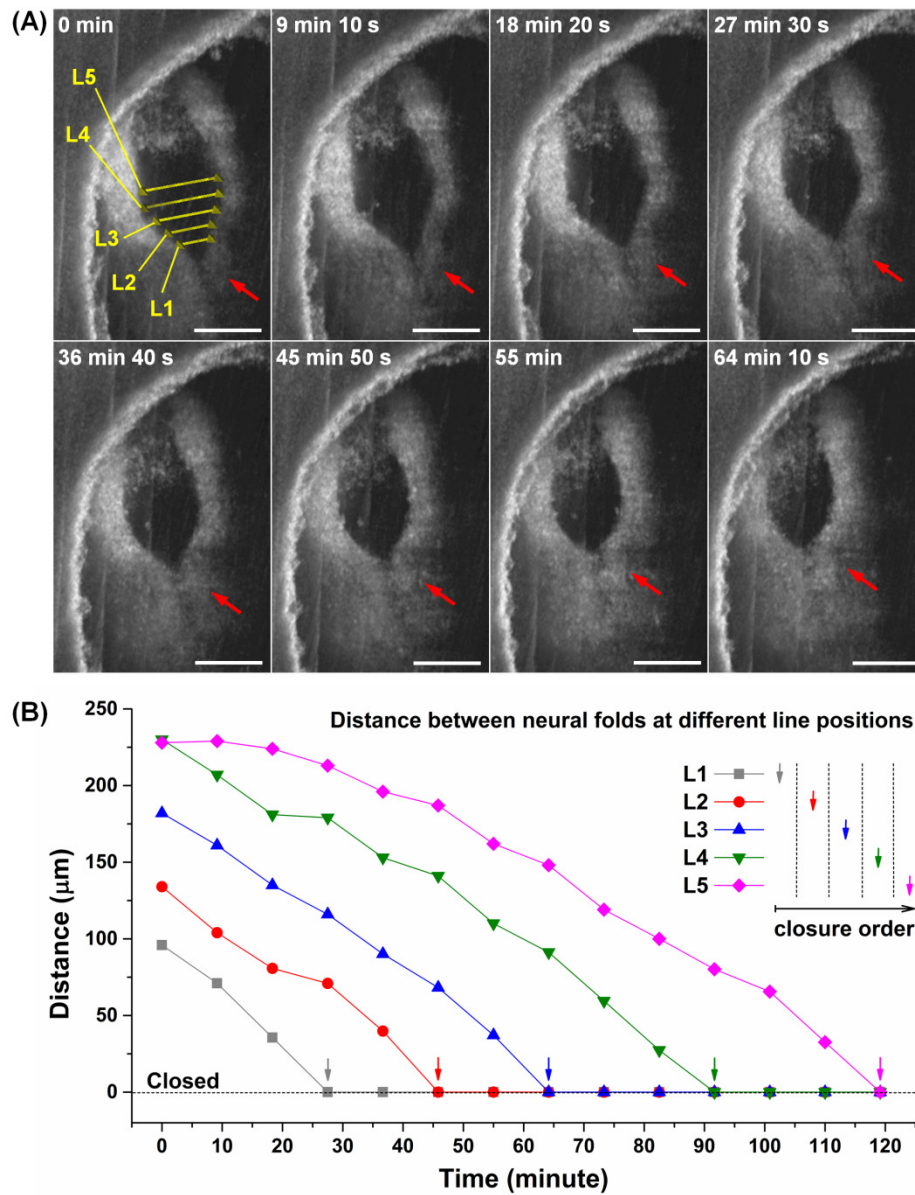


Fig. 3. Zipper-like closure of neural tube at the hindbrain region of the mouse embryo. (A) Time-resolved 3D OCT images of the mouse embryo hindbrain region show a zipper-like neural tube closure (see [Visualization 2](#)). The red arrows point at the site where zipper-like closure occurs. The yellow lines between the head folds (0 min) represent the positions where distances are measured. (B) Distances between neural folds at different line positions plotted over time indicate the zipper-like process of neural tube closure at the hindbrain region. Scale bars correspond to 200  $\mu\text{m}$ . The time stamps of images correspond to [Visualization 2](#). The playback is 5000 times faster.

In contrast to the hindbrain region, an analysis of neural tube closure in the midbrain region reveals a distinctly different mechanism. As shown in Fig. 4(A) and [Visualization 3](#), the closure of the midbrain region does not show the zipper-like continuous progression of fusion. Instead, the neural folds approach each other in a more simultaneous manner. A number of “bumps” can be seen gradually emerging from the neural folds, as indicated by red arrows. These bulging structures separately located along the neural folds appear to be the

fusion points during the closure of the midbrain region (174 minute 10 second, 183 minute 20 second, and 192 minute 30 second), suggesting a button-like closure mechanism. This process is quantitatively presented with the neural fold distances over time in Fig. 4(B). A total of eight line positions were selected to show the closure at the midbrain region, as labeled in the first panel of Fig. 4(A). It can be clearly seen that the closure order follows a button-like pattern.

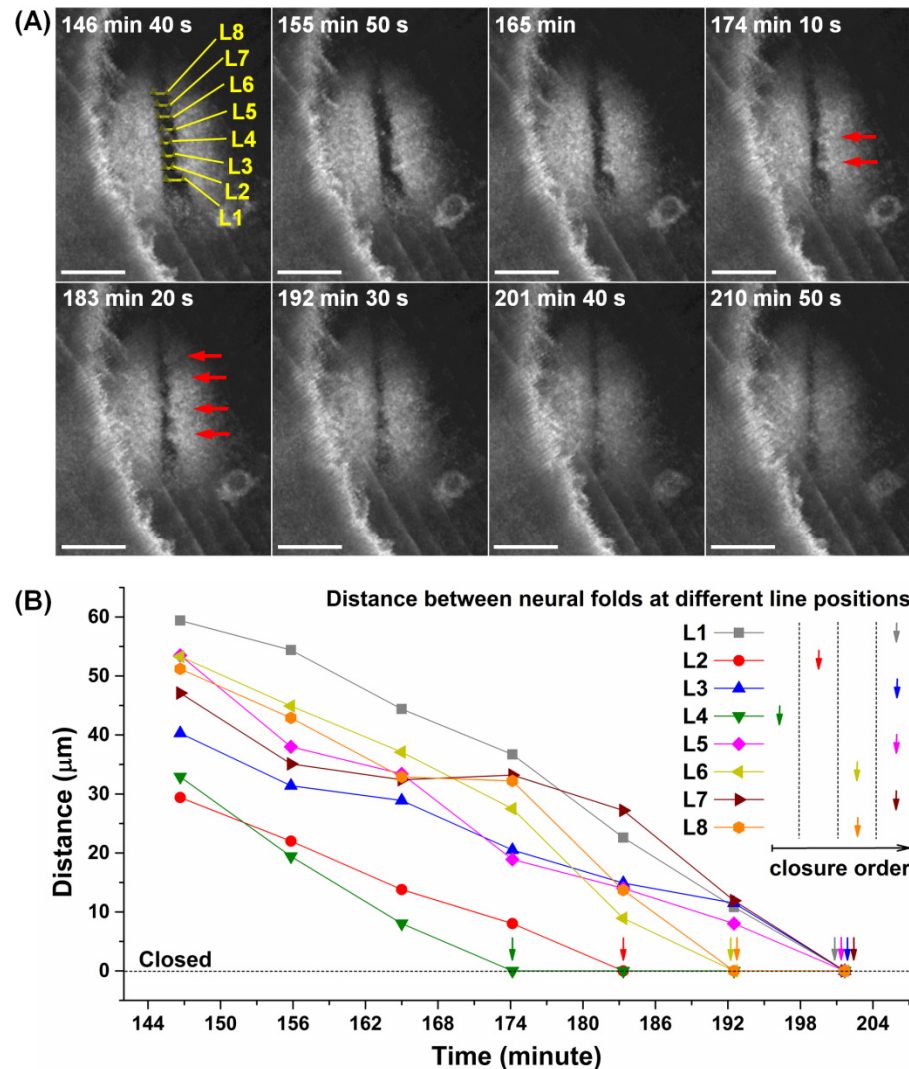


Fig. 4. Button-like closure of neural tube at the midbrain region of the mouse embryo. (A) Time-resolved 3D OCT images of the mouse embryo midbrain region show a button-like neural tube closure (see Visualization 3). The red arrows point at the sites where button-like closure occurs. The yellow lines between the head folds (0 min) represent the positions where distances are measured. (B) Distances between neural folds at different line positions plotted over time indicate the button-like process of neural tube closure at the midbrain region. Scale bars correspond to 200 μm. The time stamps of images correspond to Visualization 3. The playback is 5000 times faster.

To explore the use of OCT imaging for phenotypic characterization of NTDs, we performed 3D structural analyses of the *Wdr19* mutant mouse model. The forebrains of the control and the *Wdr19* mutant mouse embryos (E8.5, 8-12 somites) are shown in Fig. 5(A)

and Fig. 5(B), respectively. The OCT structural images provide clear 3D visualizations of the head folds from cross-sectional ventral and anterior views. The differences in neural tube closure at the forebrain can be clearly distinguished between the control and the *Wdr19* mutant embryos. Our measurements of the distance between neural folds (around the middle region of forebrain) are presented in Fig. 5(C). With 10 embryos from each group, the effect size (Cohen's  $d$ ) is over 3, indicating a large difference between the two group means. A two-sample  $t$  test with a type I error  $\alpha = 0.01$  shows a  $p$  value of less than 0.001, suggesting a statistically significant difference. The variation of data in each group is largely due to slight variations in the developmental stages between the embryos.

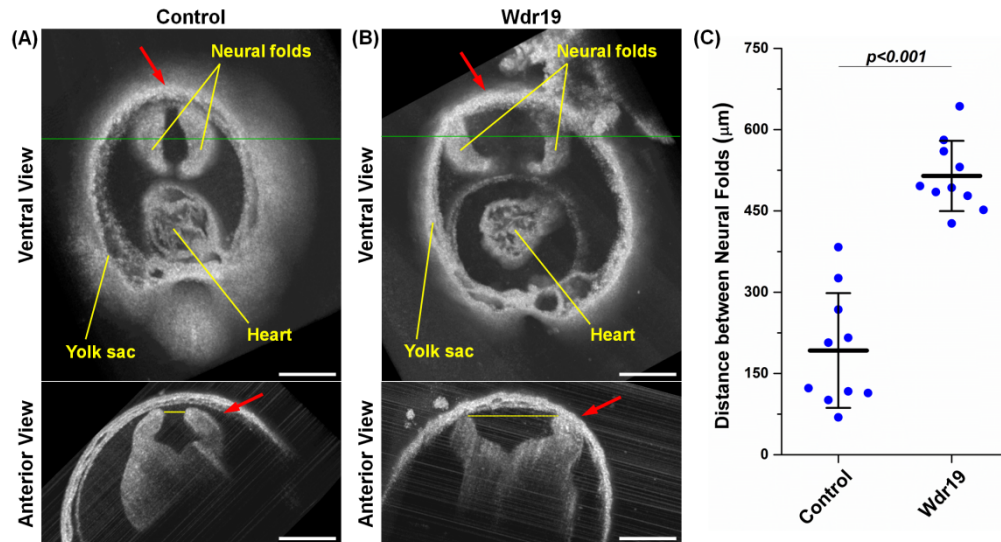


Fig. 5. Phenotypic characterization of neural tube closure at the forebrain of the *Wdr19* mutant mouse embryo. 3D OCT images of the forebrain region from the (A) control and (B) *Wdr19* mouse embryos at E8.5 show a clear difference in the neural tube phenotype. The red arrows point at the forebrain region. The green lines in the ventral views indicate the locations where the anterior views are taken. The yellow lines in the anterior views show the positions of distance measurement. All scale bars correspond to 300  $\mu\text{m}$ . (C) Quantification for the distance between neural folds at the forebrain region of the embryos show a larger distance (statistically significant) from the *Wdr19* embryos in comparison with the control. The central thick lines represent the mean and the whiskers represent the standard deviation. The number of samples  $N = 10$  for both groups. The  $p$  value is from a two-sample  $t$  test.

#### 4. Discussions and conclusions

The zipper-like closure of hindbrain in the mouse was previously reported in a number of studies [15, 21, 22] and is considered as the mechanism of the neural tube closure [12]. In our OCT imaging analysis, the zipper-like mechanism of hindbrain closure is well resolved and is clearly presented with quantitative assessment (Fig. 3 and Visualization 2). While closure of hindbrain was largely investigated due to its dorsal-side location that can be easily approached with confocal microscopy, midbrain closure was not extensively studied before. In contrast to the hindbrain, our imaging data indicates a distinct process, a button-like closure, in the midbrain region (Fig. 4 and Visualization 3). Previously, Pyrgaki et al. identified this process using fluorescence-based confocal imaging and described it as a “buttoning-up” closure with highly-dynamic cellular activities in the closure region [21]. Based on their cellular analysis [21], the “bumps” seen with OCT imaging (red arrows, Fig. 4) are likely to be cellular extensions from non-neural ectoderm cells. This consistency of our observations with the previous study indicates that OCT imaging with live embryo culture is capable and reliable for dynamic assessment of the mouse cranial development. The reason of

having two different closure mechanisms from the hindbrain and midbrain regions and how they are regulated at the molecular level deserve further investigations. While confocal microscopy allows for cellular-level contrast and resolution, OCT offers advantages of larger field of view, deeper penetration, and no requirement for fluorescent labeling, enabling an efficient morphological analysis of the mouse neural tube closure within the intact yolk sac, which was not reported possible with other imaging techniques.

A mutation in *Wdr19* (or known as *Ift144*) in mice was previously reported to cause brain abnormalities characterized at a later embryonic stage [61]. Our quantitative analysis of the mouse forebrain reveals a significant difference in the distance between neural folds at E8.5 for the *Wdr19* homozygous embryos in comparison to the control littermates. Our assessment enabled by OCT imaging complements the previous characterization. Since *Wdr19* mutants are predicted to have alterations in ciliary structure and/or function, the revealed neural tube defect in *Wdr19* mutants suggests a possible role that cilia might play in the process of neural tube closure. Further studies involving the characterization of cilia behavior at the earlier developmental stages are required to pursue this question.

The pixel scales of our dynamic OCT imaging are  $\sim 2\ \mu\text{m}$  in the axial direction and  $\sim 3\ \mu\text{m}$  in the transverse direction. Based on our results, this spatial sampling rate is sufficient to capture detailed structural information from the head folds, such as the bulging structures in the midbrain closure. An improved transverse sampling can be easily achieved, however, with increasing the size and the acquisition time of the volume data. The axial resolution of OCT is decoupled from the transverse resolution and is only dependent on the laser wavelength and bandwidth [62]. Extending the wavelength range of the imaging light will further enhance the depthwise resolving ability, for example, to the single-micron level [63]. Also, improvement of the transverse resolution can be obtained by using a microscopy scheme [64, 65] where a higher magnification lens is utilized. Potentially, such system enhancements could help to achieve finer morphologic analysis of the head folds in the embryo and might reveal other structural features useful for neural tube analysis.

In the time-lapse OCT 3D imaging, resampling of time in post-processing was performed to reduce the size of the 4D data set and improve the visualization efficiency. However, a 3D temporal resolution of 110 seconds ( $\sim 9\ \text{Hz}$  B-scan rate) is available to reveal more transient structural activities during mouse neurulation. Also, using a higher A-line rate of our OCT system, the volume with similar spatial sampling intervals can be acquired within 20 seconds, which could potentially be used to capture even more detailed neural tube morphogenesis within specific time windows. With the rapid and continuous advancements in electronics, real-time 3D OCT imaging and visualization has recently been demonstrated [66], which can potentially provide more efficient characterization of mouse embryonic cranial phenotypes.

Although the process of cranial neural tube closure can be directly visualized from the 3D OCT images, we believe the time-resolved measurement of neural fold distances at different locations provides an additional quantitative description of the closure, which clearly presents the distinct mechanisms from the midbrain region and the hindbrain region. This type of 3D measurements can be further used to assess other parameters, such as the moving speed of head folds and the progression velocity of zippering, which might be useful measures for future characterization of abnormal neural tube dynamics. With an improved spatiotemporal resolution, assessment of specific closure feature between the intermediate buttoning points in the embryonic midbrain region may contribute to a more comprehensive understanding of cranial morphogenesis in the mouse.

In conclusion, we have presented the first study demonstrating the feasibility of OCT for live imaging and analysis of cranial neural tube closure in the mouse embryo. We report time-lapse 3D OCT imaging results on head fold closure and specifically show the button-like closure in the midbrain region which is distinct from the zipper-like closure in the hindbrain region. The temporally and spatially resolved measurements of the distance between neural folds support the observation and clearly indicate the closure mechanisms from a quantitative



point of view. Our results from the analysis of the forebrain neural fold distances in Wdr19 mutant mouse embryos demonstrate that OCT can provide the phenotypic characterization of defects in the mouse neural tube development. We expect that our approach and the findings from this work will facilitate novel studies to address the etiology of human NTDs.

### **Funding**

This work was supported by the National Institute of Health grants R01HL120140 (I.V.L), R01HD086765 (K.V.L), U54HG006348, and R25GM056929, as well as by the American Heart Association grant 16POST30990070 (S.W.).

### **Acknowledgments**

We would like to thank the support from the Optical Imaging and Vital Microscopy Core at Baylor College of Medicine.